Supplement of Hydrol. Earth Syst. Sci., 26, 375–395, 2022
https://doi.org/10.5194/hess-26-375-2022-supplement

Hydrology and Earth System Sciences
Open Access
EGU

Supplement of

Climatic and anthropogenic drivers of a drying Himalayan river

Gopal Penny et al.

Correspondence to: Gopal Penny (gopalpenny@gmail.com)

Contents

S1 Streamflow integrity checks and baseflow separation

To ensure reliability of data from each stream gauge, we prepared pairwise double-mass plots between gauges using median streamflow from each month and finding that all gauges were consistent with at least one adjacent gauge (see Figure S1). To further ensure temporal and spatial consistency, we sampled three observations per month for each gauge, selected to be evenly spaced throughout the month. We then calculated subcatchment streamflow at each gauge by subtracting streamflow from the gauge directly upstream. The full results are presented in Figure S2.

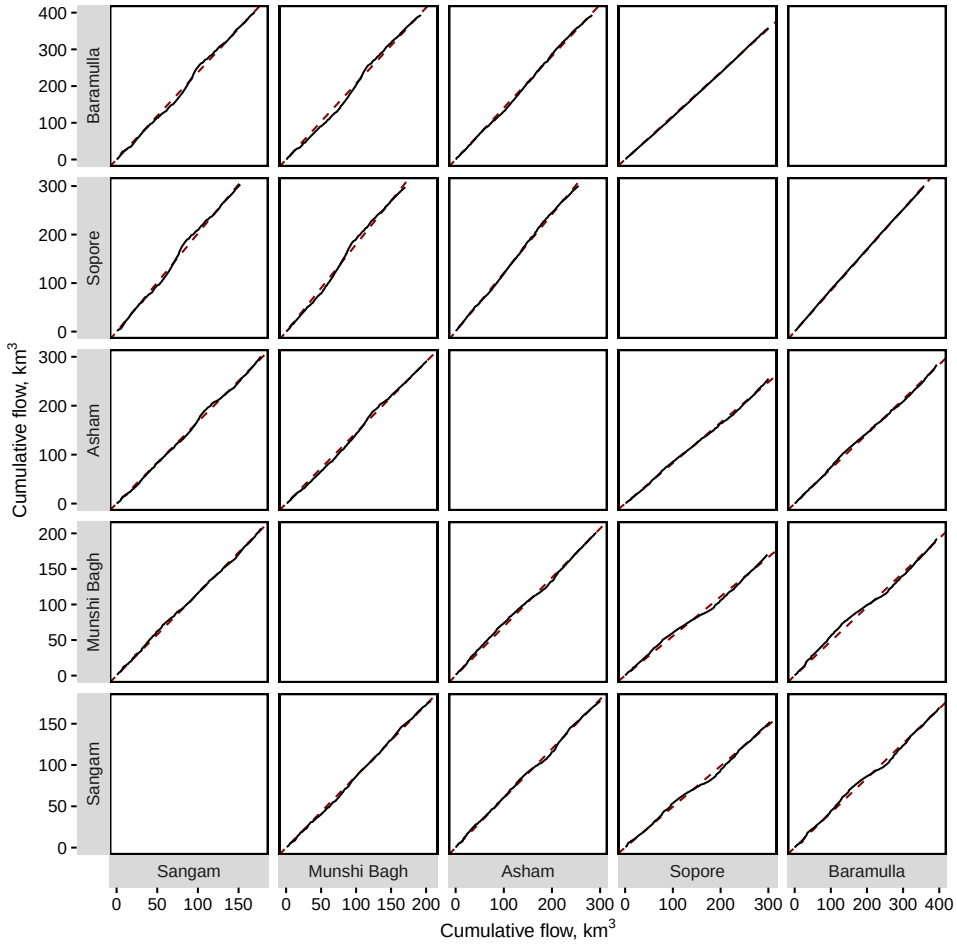

Figure S1: Pairwise double mass curves for median monthly streamflow across each of the 5 gauges from 1960 through 2013. Each gauge compares well with the neighboring gauge, with the order from downstream to upstream being Baramulla–Sopore–Asham–Munshi Bagh–Sangam. The red dashed line represents the least-squares best slope, and provides a reference for the linearity of the curve.

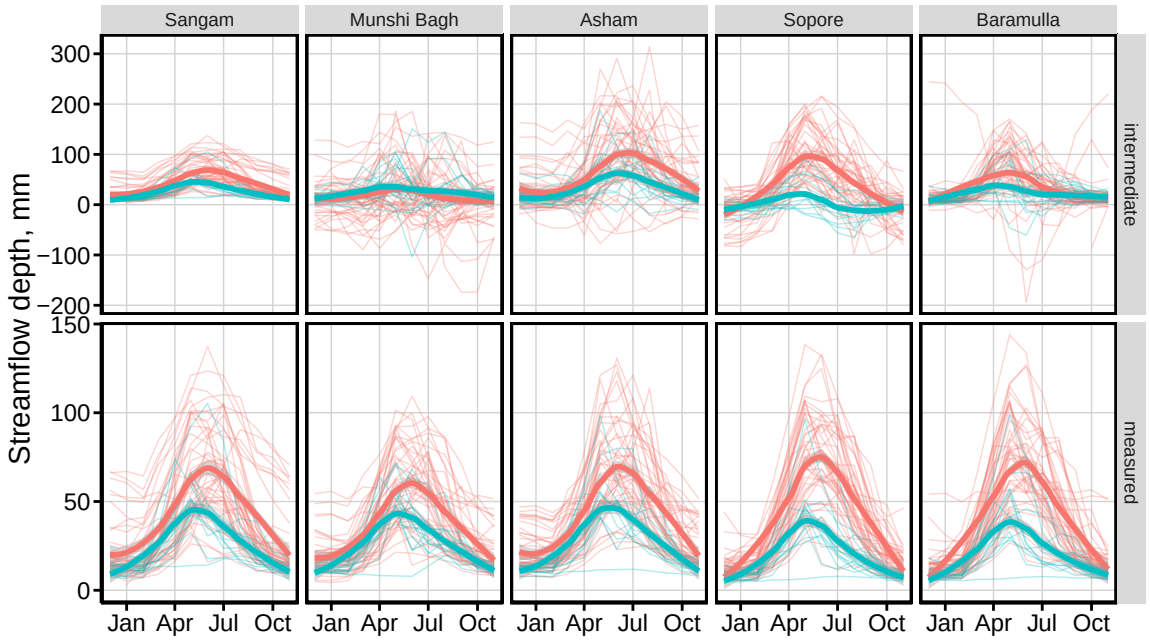

Figure S2: Intraannual baseflow at all five gauges before (red) and after (blue) 2000. Observations for all years are included in thin, semi-transparent lines, with the smoothed average shown in thicker dark lines. The figure includes baseflow calculated at each gauge ("measured," bottom) and the that calculated as inflow from the "immediate" subcatchment of the gauge (calculated by subtracting baseflow at the upstream gauge, top).

Using the three-monthly streamflow dataset, we conducted baseflow separation using a numerical filter (Nathan and McMahon, 1990) and then aggregated baseflow, quickflow, and total streamflow to monthly, seasonal, and annual values. The baseflow separation calculated from trimonthly streamflow compared well with baseflow from daily streamflow (see Figs S3 & S4) and, importantly, ensured temporal consistency across all gauges.

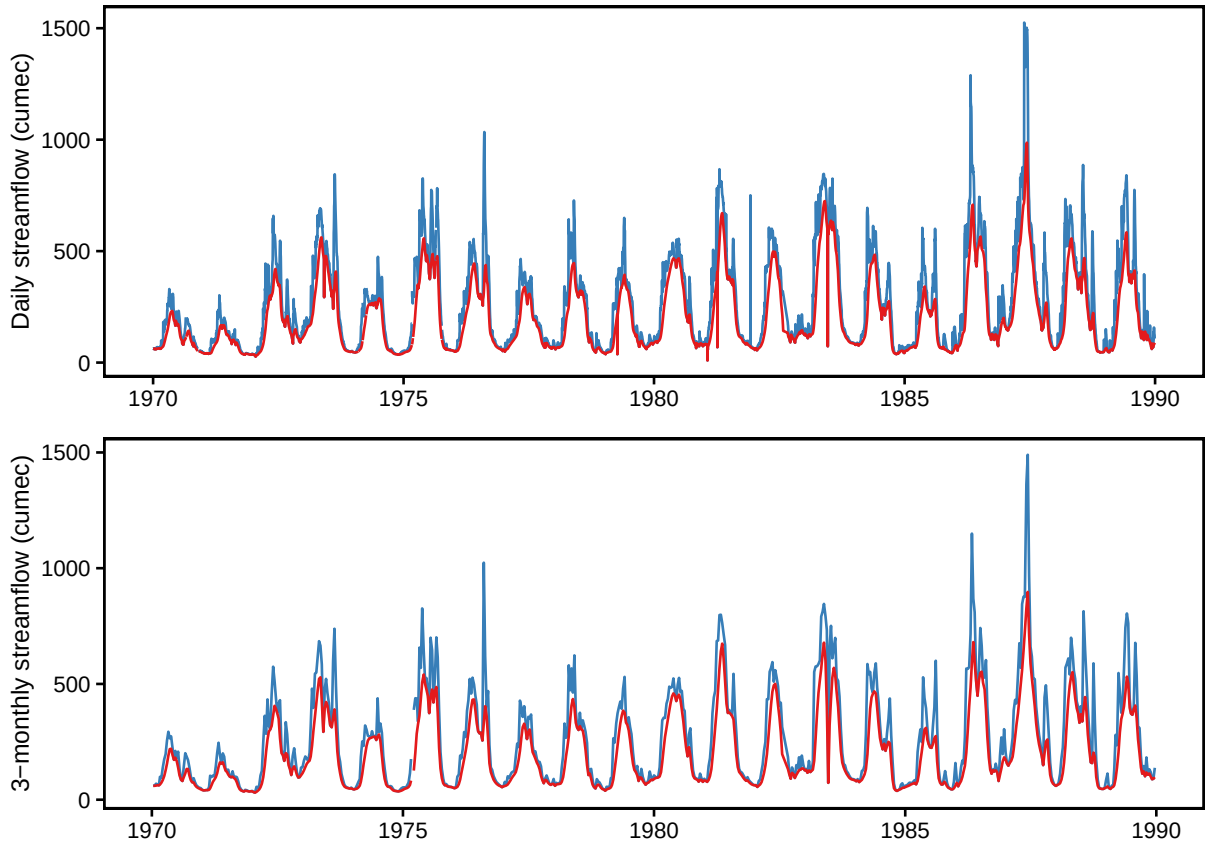

Figure S3: Baseflow separation. (top) Baseflow separation using a digital recursive filter (Nathan and McMahon, 1990) on daily streamflow values at the most downstream station at Baramulla. The filter parameter was set to $\alpha = 0.925$, in accordance with (Nathan and McMahon, 1990). (bottom) Baseflow separation using the same digital recursive filter on three-monthly flow. The filter parameter was manually tuned to $\alpha = 0.45$ so that the annual baseflow index matched from three-monthly streamflow matched the baseflow index from daily streamflow (see Figure S4).

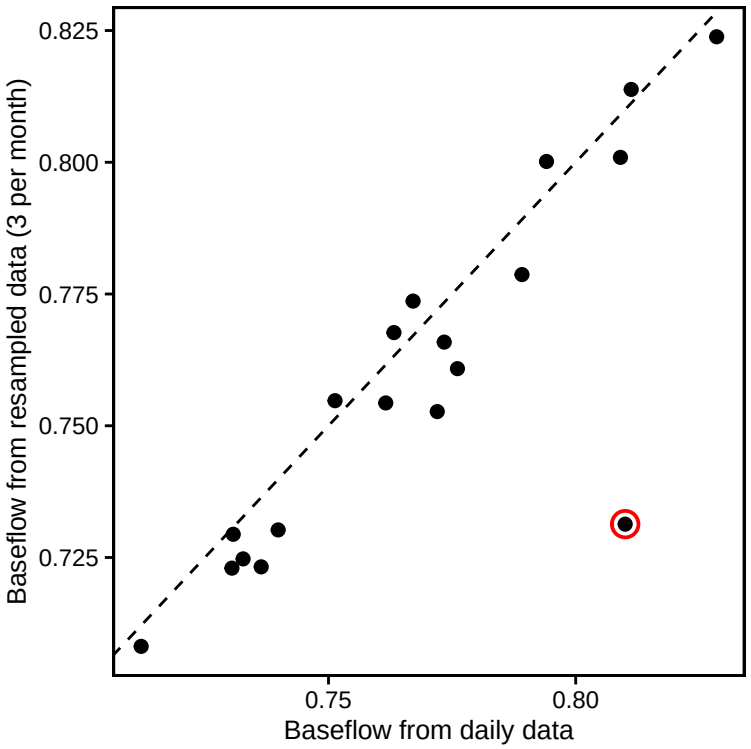

Figure S4: Comparison of annual baseflow determined from daily streamflow (x-axis) and three-monthly streamflow (y-axis). The point circled in red is from 1983 and biased downwards due to an anomaly in the flow data (see Figure S3). The correlation between the two datasets increased considerably when discarding the value from 1983 ($R^2 = 0.72$ including all points, $R^2 = 0.95$ excluding 1983).

S2 Precipitation interpolation and uncertainty

As an alternative to Thiessen polygons, we also applied an elevation gradient with inverse-distance weighting to regionalize gauged precipitation. To determine basin precipitation using an elevation gradient, we first fit linear precipitation-elevation curves for each year-season combination using ordinary least-squares regression. We then determined a pre-2000 and post-2000 elevation gradient, taken as the mean elevation gradient within each season. As a robustness check, we ran t-tests to determine if the difference in means was statistically significant. For instance, the pre-2000 summer elevation gradient was 0.29 mm m^{-1} compared to a gradient of 0.17 mm m^{-1} for the post-2000 summer period, with the t-test indicating a statistically significant difference ($p = 0.23$). The remaining seasons did not exhibit a statistically significant difference in the elevation gradient. However, we ultimately decided to use the (more parsimonious) Thiessen interpolation because it better captures the net outgoing fluxes of the water balance (i.e., streamflow plus ET) before (-14%) and after ($+16\%$) 2000. In contrast, the elevation gradient approach overestimated these fluxes considerably ($+43\%$ and $+93\%$, respectively). We therefore take the Thiessen interpolation as a more reliable approach for estimating watershed precipitation. The spatial differences in the interpolation methods are presented in Fig. S5. To contrast the outcomes of the two interpolations please see Fig. S6 below, which reproduces Fig. 4 from the main text but using the elevation-gradient interpolation instead of the Thiessen polygon interpolation.

Lastly, we note that the annual decrease in precipitation was comparable across all three observation stations: -158 mm at Kupwara (northwestern station), -96 mm at Srinagar station (middle station), and -129 mm at Pahalgam (southeastern station). The Pahalgam station is at the highest elevation (approximately 2700 m), while the Kupwara and Srinagar stations are at lower and comparable elevations (1600 m).

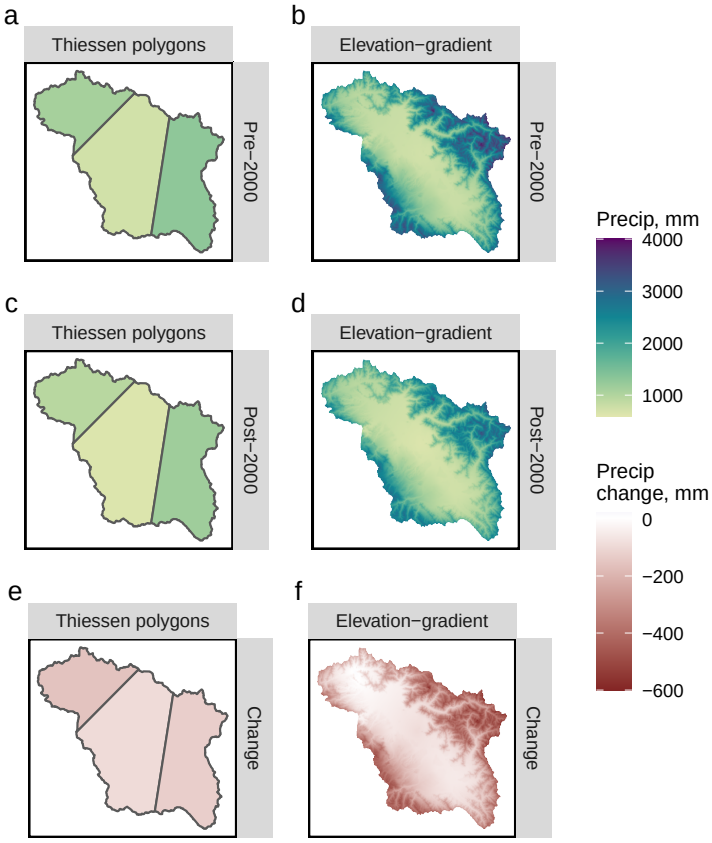

Figure S5: Precipitation interpolation using Thiessen polygons (left) and inverse distance squared with an elevation gradient (right), including (a, b) Pre-2000, (c, d), Post-2000, and (e, f) the change between the two periods. Given the difficulty of measuring precipitation in regions with strong elevation gradients and significant snowfall, we used a water balance closure to interpret the validity of the two methods. In both periods (pre- and post-2000), the Thiessen polygon approach yields less uncertainty in the water balance closure.

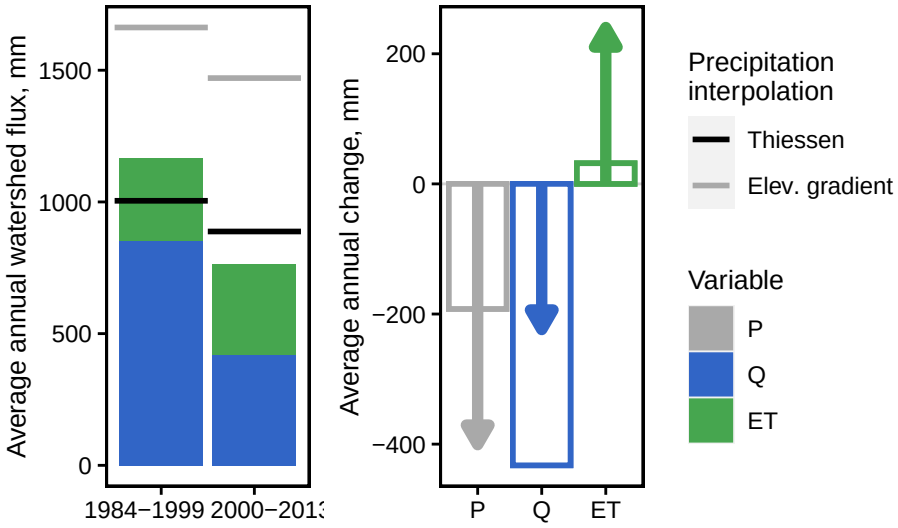

Figure S6: Water balance for the Upper Jhelum, similar to Fig. 4 in the main text but with precipitation interpolated using the elevation gradient approach. (left) Average annual fluxes (P, Q, and ET) for the periods 1984–1999 and 2000-2013, including both type of precipitation interpolation: Thiessen polygon and elevation gradient. (right) Average annual *change* in water balance fluxes between the two periods, given by the bars, with each flux estimated independently. The change in water balance fluxes estimated from water balance residuals is given by the arrows, with precipitation estimated from the elevation gradient approach. In other words, each flux is calculated using the equation $\Delta P_{elev} - \Delta Q - \Delta ET = 0$ and estimates of the other two fluxes. The elevation gradient interpolation does a better job at closing the residual water balance than Thiessen polygon approach, but considerable error remains (as given by the different between the arrows and bars) and the conclusions drawn from each approach are similar.

Additionally, in order to ensure that our analysis of the distribution of storm sizes was not sensitive to the minimum storm size (2 mm), we re-ran the analyses described in Section 3.2.2 of the main text using minimum storm sizes of 1 mm and 3 mm (see Table S1).

Table S1: Robustness check for a change in the distribution of precipitation event sizes. The same analyses were run as described in the main text (Sect. 3.2.2), with minimum storm sizes of 1 mm and 3 mm. The event size bins for 1 mm were: small (1–6.4 mm), medium (6.4–17.4 mm), and large (≥17.4 mm) events. The event size bins for 3 mm were: small (3–8.4 mm), medium (8.4–20.1 mm), and large (≥20.1 mm) events.

Hyp.	Change in:	Min event size	Conf. int	Sig
3	Number of large events	1 mm	[-4.1, -2.7]	Y
	Number of medium events	1 mm	[-0.2, 2.2]	
	Number of small events	1 mm	[31.2, 36.7]	Y
	Number of large events	3 mm	[-3.6, -2.4]	Y
	Number of medium events	3 mm	[-0.8, 1.1]	
	Number of small events	3 mm	[6.0, 9.1]	Y

S3 ET regression analysis

The ET regression was run on 500 m pixels sampled on a 2.5 km grid to determine a_s, after which ET was predicted for all Landsat pixels at 480 m. To conduct the analysis, multiple satellite products were prepared and downloaded from Google Earth Engine, including 500 m MODIS ET and 480 m pyramid pixels of Landsat 5 and 7 NDVI calculated from surface reflectance. Both products were sampled on the same 2.5 km grid. Although the pixels did not perfectly align, the processing speed was increased dramatically by sampling Landsat pixels at 480 m rather than reprojecting and resampling Landsat to the MODIS resolution. Furthermore, the correlation of Landsat NDVI between the MODIS resolution and the 480 m sampling was high ($R^2 = 0.94$).

Temperature data was obtained from IMD-Srinagar at Pahalgam (monthly), Srinagar (daily), Qazigund (daily), and Gulmarg (daily) stations. We interpolated temperature across the watershed using inverse-distance weights and applied seasonal adiabatic lapse rates to adjust for elevation differences (see Dodson and Marks, 1997; Stahl et al., 2006, for details). Lapse rates ranged from 6.12 °C/km in winter to 8.58 °C/km in spring and were close to expected ranges for the climate and latitude (Stone and Carlson, 1979).

We determined the a_s and c coefficients using observations from the 2.5 km grid and nonlinear least-squares regression. The NDVI exponent was fit to $c = 0.81$, giving confidence in the regression and the diminishing relationship between NDVI and stomatal conductance at high NDVI. Evapotranspiration was then predicted for all 480 m Landsat pixels directly from Eq. 2 (main text) using long-term seasonal averages of NDVI before and after 2000.

For the pre-2000 summer period, some pixels contained few (<5) clear-sky Landsat images. The pixels tended to be at high elevations along ridges where cloud cover was more likely (see Fig. S7).

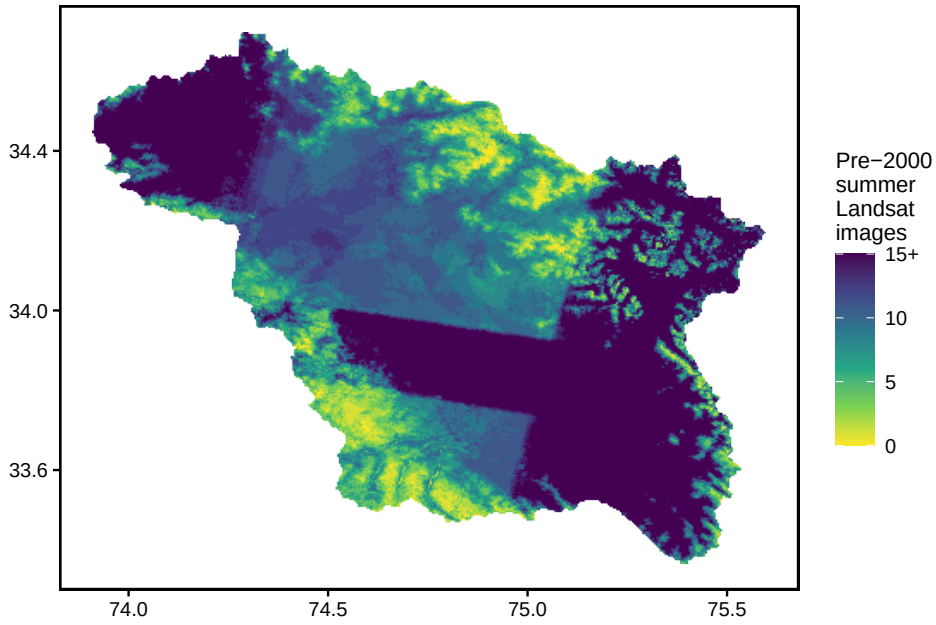

Figure S7: Number of pre-2000 clear-sky summer images at each pixel throughout the Upper Jhelum watershed. Higher elevations are more likely to be hidden by clouds and therefore be captured in fewer images.

To ensure the effect of these pixels did not bias the results, we considered histograms of the number of clear-sky images on a per-pixel basis (Fig. S8). A small portion (14%) contained ≤5 clear-sky images.

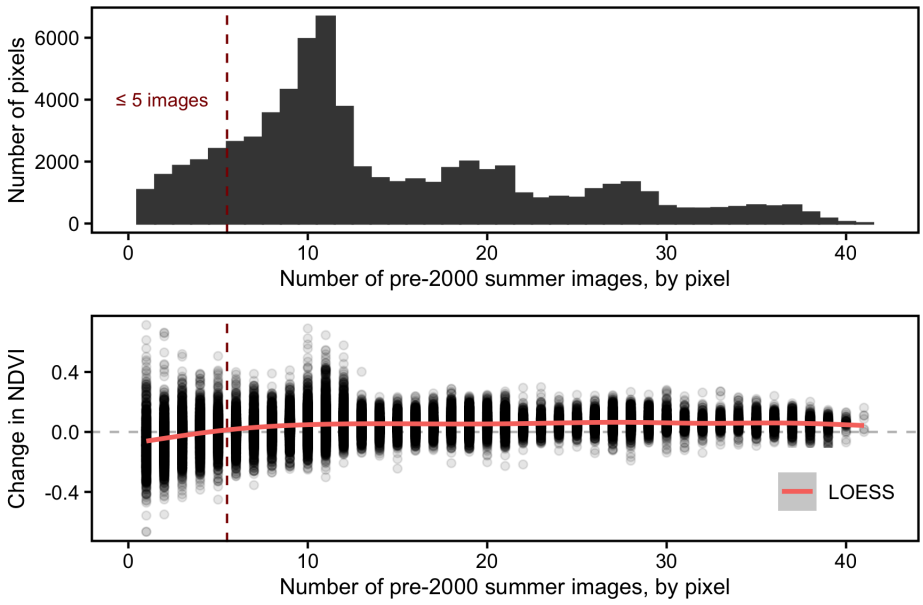

Figure S8: Histogram of pre-2000 clear-sky summer images at each pixel (top). NDVI change (from before to after 2000) versus the number of clear-sky summer images in each pixel (bottom). As shown by the moving (LOESS) regression, NDVI was insensitive to the number of clear-sky images except when the number of images was less than or equal to 5. These pixels account for 14% of the watershed, and therefore have a small effect on watershed-average NDVI.

S4 Additional Figures

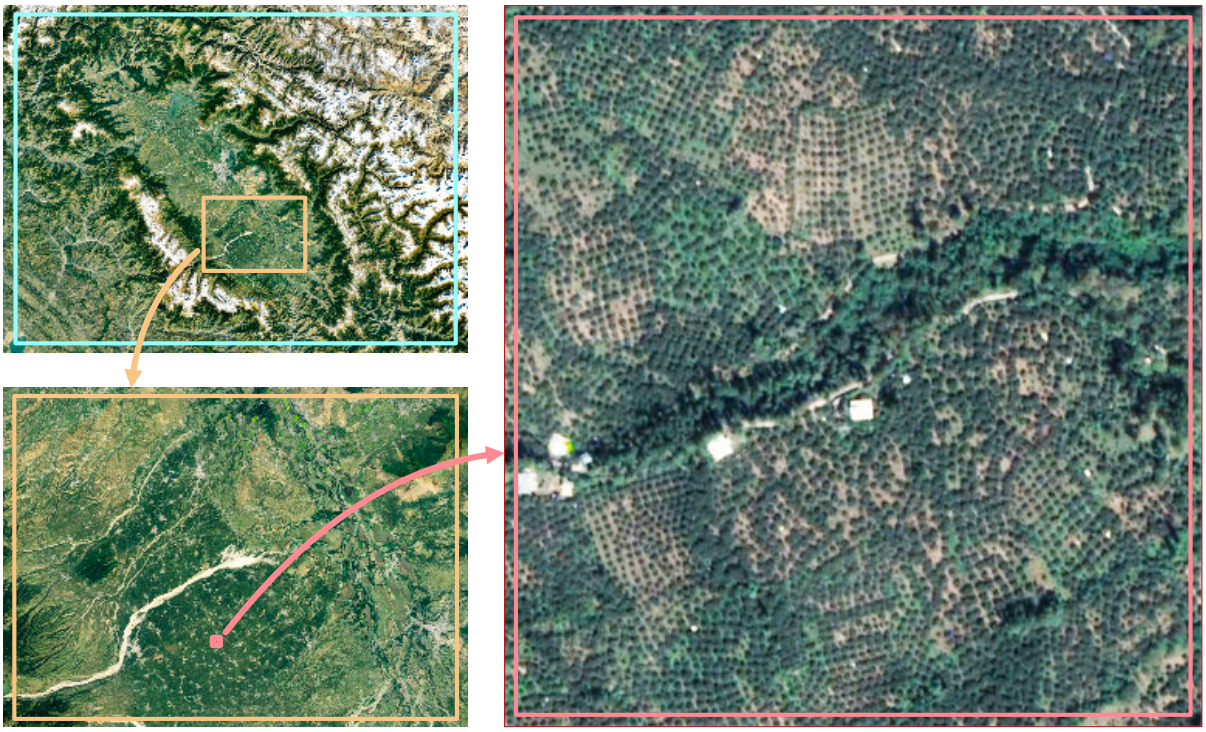

Figure S9: Visual inspection of satellite imagery from Google Earth (©2021 Google, ©2021 Maxar Technologies) in the southern portion of the Upper Jhelum confirms that the MODIS land use classification of mosaic vegetation represents orchards, seen throughout the right image as gridded sowing of trees.

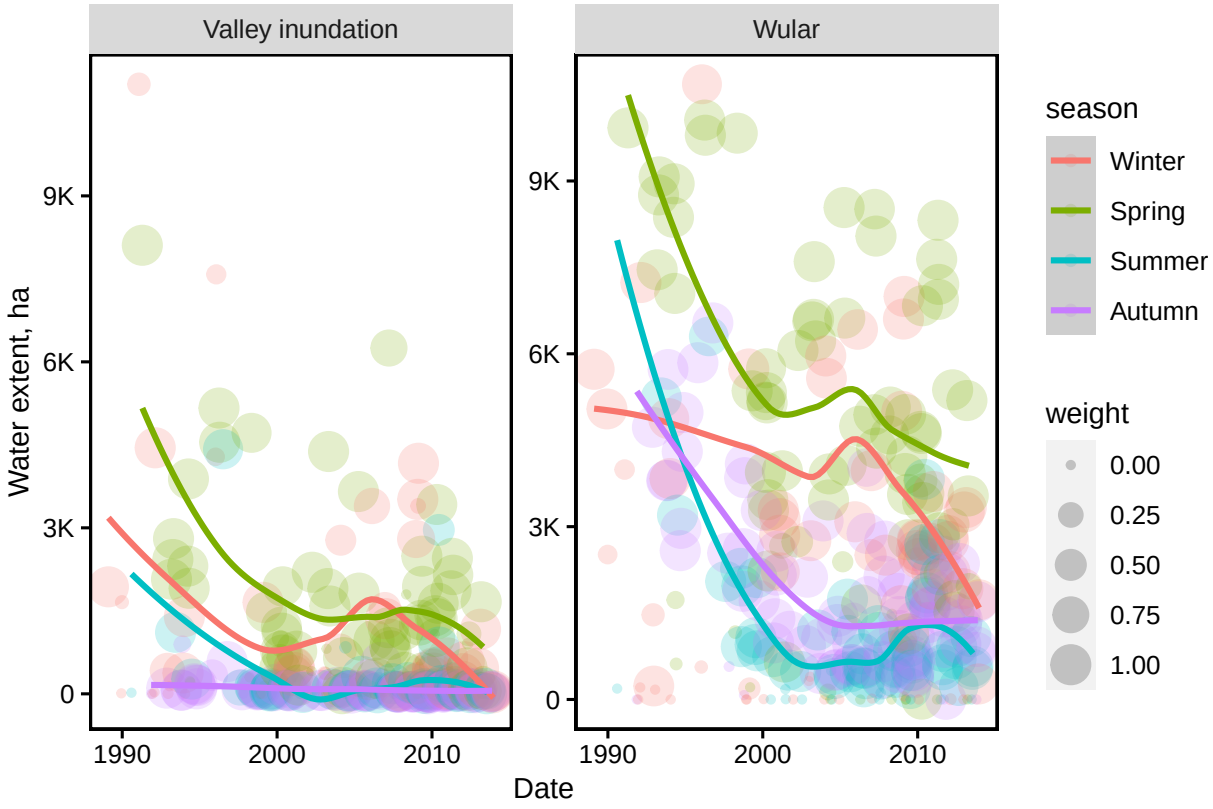

Figure S10: Open water extent classified from Landsat 5 and 7 imagery declined across all four seasons in Wular Lake and as exhibited by valley inundation. The curves are determined using locally estimated scatterplot smoothing (LOESS) regression. We gave more credibility to images in which there the cloud area was small in comparison to the water area, and therefore weighted individual observations by the ratio of the area of clouds over the area of water as $\exp(-A_{clouds}/A_{water})$.

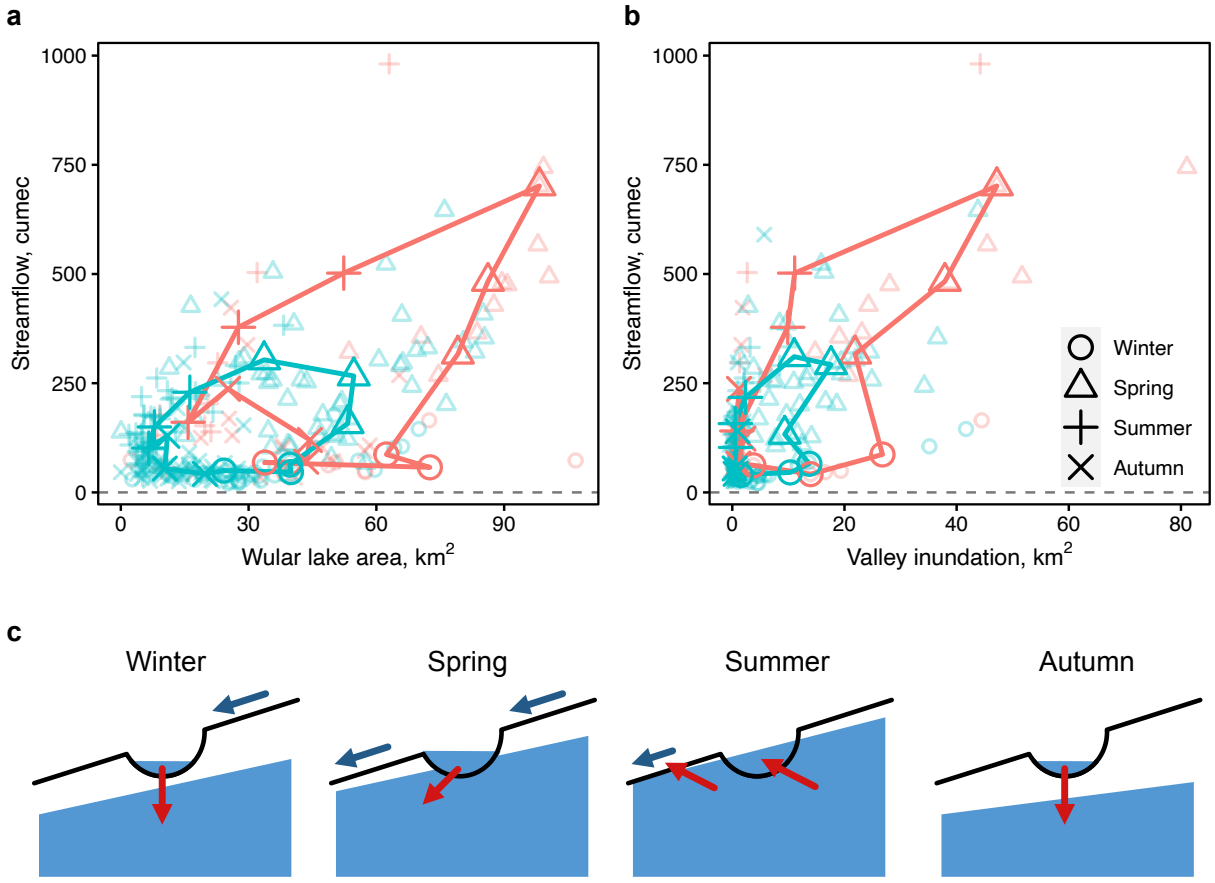

Figure S11: Streamflow (cumec, or $m^3\ s^{-1}$) versus water extent (km^2) at Sangam station for Wular lake (a) and valley inundation (b), before (red) and after (blue) 2000. Each observation is shown as a small, semi-transparent marker. Monthly averages are presented in large markers connected by lines. The top-right triangle (in red, both sides) represents May, followed by the first summer month (June). (c) Hypothesis to explain how groundwater, surface runoff, and surface storage could interact in different seasons to create the observed hysteresis. The figure shows losing conditions in winter, spring, and autumn and gaining conditions in the summer, once the groundwater table has been recharged from spring precipitation and snow melt.

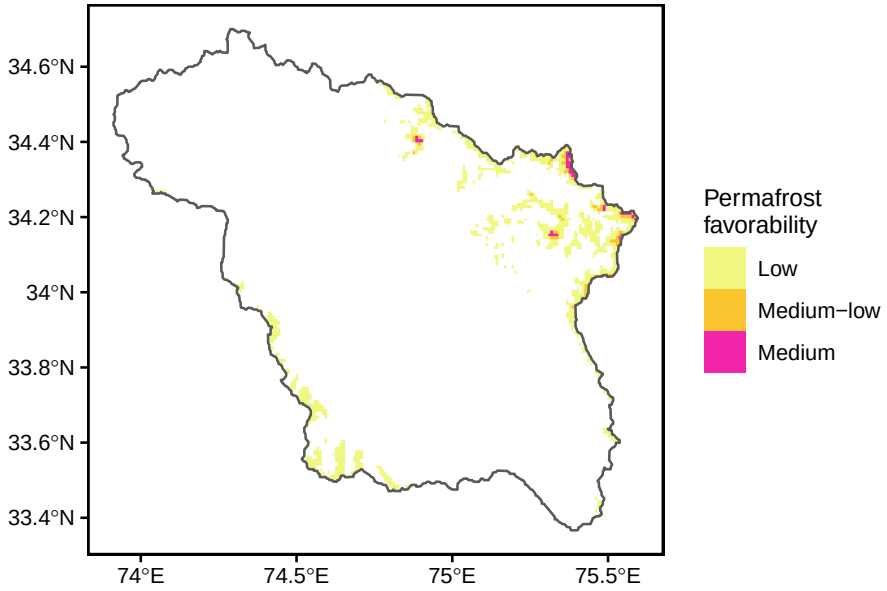

Figure S12: Permafrost likelihood from the Global Permafrost Zonation Index (Gruber, 2012). The index spans a range from a minimum of "permafrost exists only in most favorable conditions" and to a maximum of "permafrost exists in nearly all conditions." We binned this scale into five groups of permafrost likelihood including low, medium-low, medium, medium-high, and high. The highest permafrost likelihood in the Upper Jhelum watershed is medium. Roughly 0.19% of the watershed has at least a medium likelihood of permafrost. In a larger portion (6.4%) permafrost has a low likelihood.

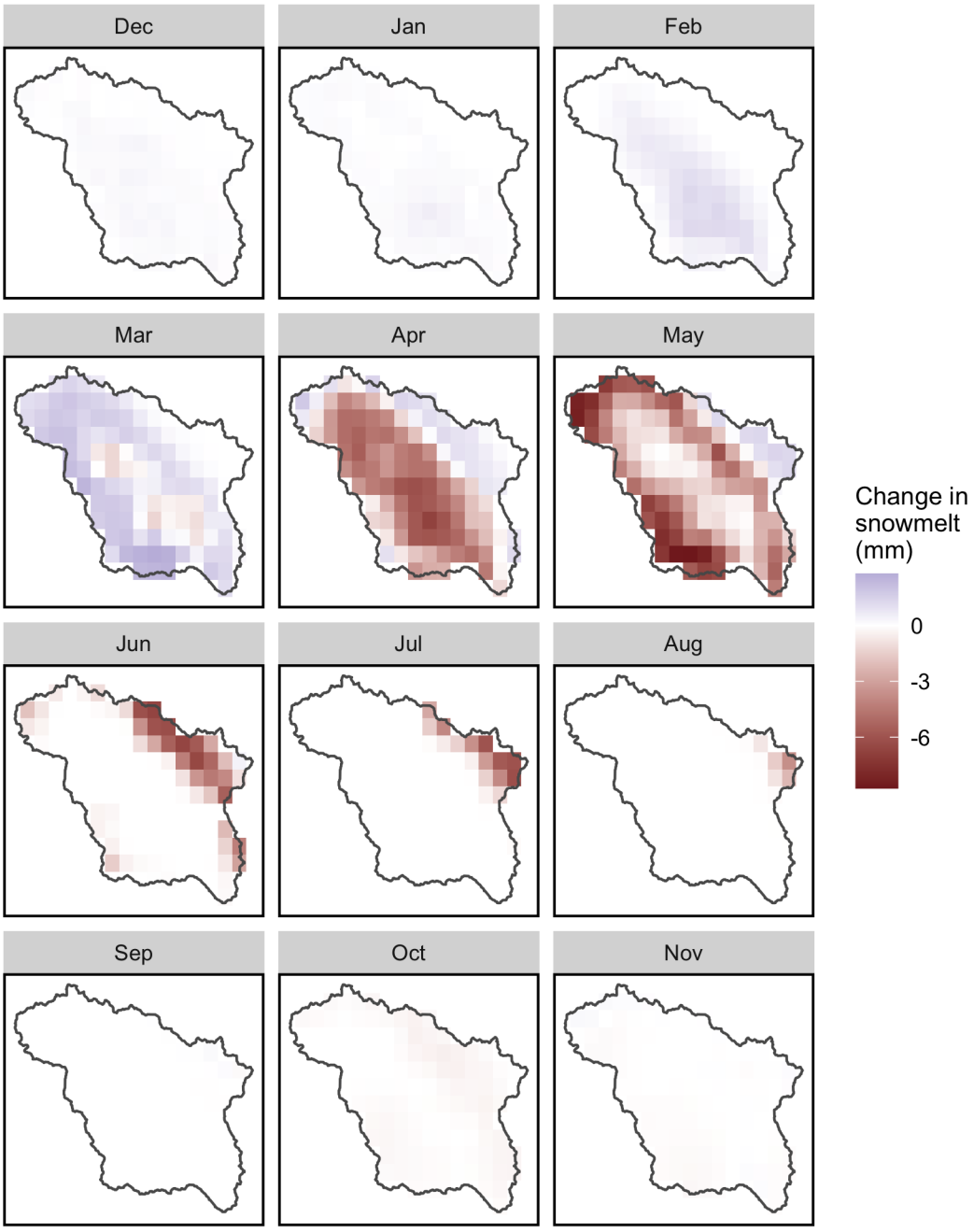

Figure S13: Change in monthly snowmelt from the ERA5-Land reanalysis dataset (Muñoz-Sabater et al., 2021), comparing the before (1984–1999) and after (2000–2013) periods across the Upper Jhelum watershed. Each row corresponds to a season (winter, spring, summer, autumn). The reanalysis yields more snowmelt in earlier months of the year and less snowmelt in later months at all elevations of the watershed.

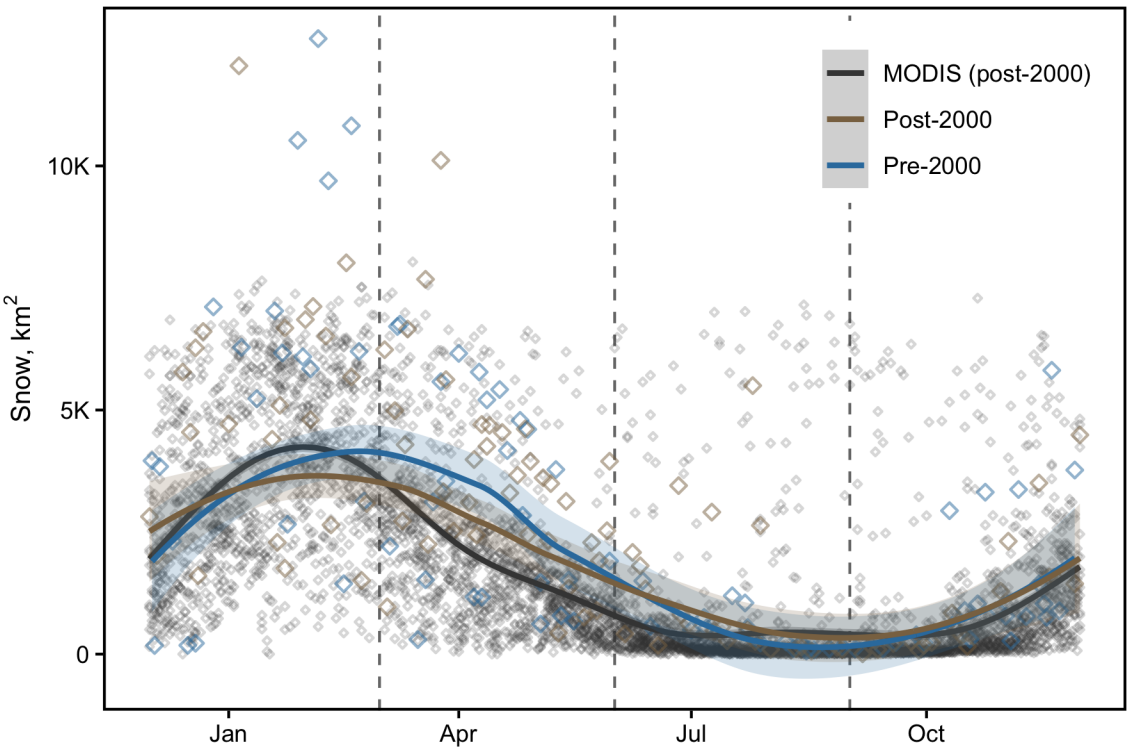

Figure S14: Smoothed intra-annual snow cover before and after 2000, including MODIS (post-2000, black) and Landsat (pre-2000 in blue, post-2000 in brown). The Landsat data were used in the formal hypothesis testing presented in the main text.

References

Dodson, R. and Marks, D.: Daily air temperature interpolated at high spatial resolution over a large mountainous region, Climate Research, 8, 1–20, https://doi.org/10.3354/cr008001, 1997.

Gruber, S.: Derivation and analysis of a high-resolution estimate of global permafrost zonation, The Cryosphere, 6, 221–233, 2012.

Muñoz-Sabater, J., Dutra, E., Agustí-Panareda, A., Albergel, C., Arduini, G., Balsamo, G., Boussetta, S., Choulga, M., Harrigan, S., Hersbach, H., et al.: ERA5-Land: A state-of-the-art global reanalysis dataset for land applications, Earth System Science Data Discussions, pp. 1–50, 2021.

Nathan, R. J. and McMahon, T. A.: Evaluation of Automated Techniques for Baseflow and Recession Analysis, Water Resources Research, 26, 1465–1473, https://doi.org/10.1029/WR026i007p01465, 1990.

Stahl, K., Moore, R. D., Floyer, J. A., Asplin, M. G., and McKendry, I. G.: Comparison of approaches for spatial interpolation of daily air temperature in a large region with complex topography and highly variable station density, Agricultural and Forest Meteorology, 139, 224–236, https://doi.org/10.1016/j.agrformet.2006.07.004, 2006.

Stone, P. H. and Carlson, J. H.: Atmospheric lapse rate regimes and their parameterization., Journal of the Atmospheric Sciences, 36, 415–423, https://doi.org/10.1175/1520-0469(1979)036⟨0415:ALRRAT⟩2.0.CO;2, 1979.